Dynamical properties of a composite microcracked bar based on a generalized continuum formulation

Valeria Settimi, Patrizia Trovalusci & Giuseppe Rega

Continuum Mechanics and Thermodynamics

ISSN 0935-1175

Continuum Mech. Thermodyn.
DOI 10.1007/s00161-019-00761-7

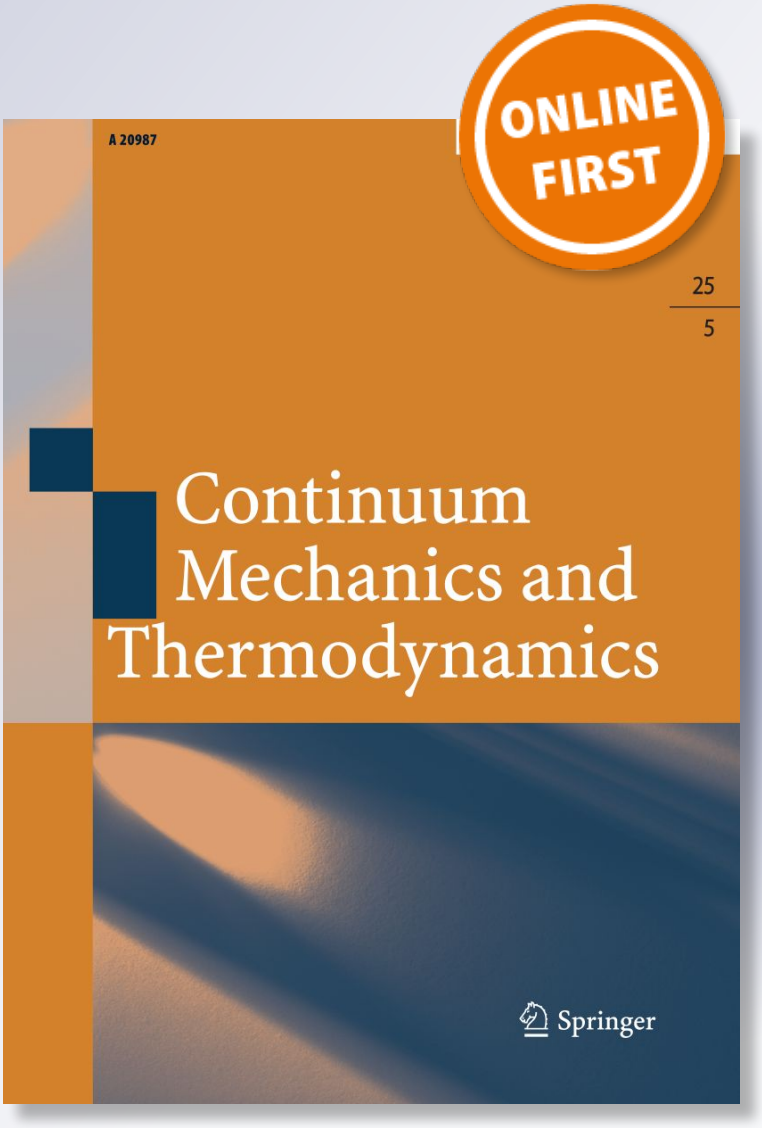

Springer

Continuum Mech. Thermodyn.
https://doi.org/10.1007/s00161-019-00761-7

ORIGINAL ARTICLE

Valeria Settimi · Patrizia Trovalusci · Giuseppe Rega

Dynamical properties of a composite microcracked bar based on a generalized continuum formulation

Received: 5 February 2019 / Accepted: 14 March 2019

Abstract The dynamical behavior of a mono-dimensional bar with distributed microcracks is addressed in terms of free and forced wave propagation. The multiscale model, derived from a generalized continuum formulation, accounts for the microstructure by means of a microdisplacement variable, added to the standard macrodisplacement, and of internal parameters representing density and length of microcracks. The influence of coupling between micro- and macrodisplacement overall response on the system is discussed, as well as the effect of the damage parameters on the propagating waves.

Keywords Multiscale-multifield models · Microcracked media · Wave propagation · Dispersion features

1 Introduction

In contemporary technological applications, wide interest is devoted to microstructured materials: e.g., composites, masonry-like and granular materials, and porous and damaged media. Such materials are characterized by the existence of an internal structure represented by material length parameters, which can account for the distance between particles, the size of a grain, the length, and distance of microcracks, etc., that introduce a scale dependence in the model governing equations.

The mechanical modeling of microstructured continua meets the main difficulty in accounting for the microscopic features through suitable constitutive laws, without resorting to the direct description of the microstructure that would result in the addition of many degrees of freedom. In this respect, a direct description of these materials in Lagrangian terms is often cumbersome [1,2] and then continuum descriptions that keep memory of the internal microstructure are often required.

Since many years, several homogenization or coarse-graining methods for deriving equivalent classical continua have been proposed in the literature also with reference to materials with random microstructure [3–7]. However, by lacking in material internal length parameters, the simple (Grade 1) classical continuum does not always seem appropriate for representing the macroscopic behavior of these materials, taking into account the size, the orientation, and the disposition of the heterogeneities. This often calls for the need of non-classical (generalized) continuum descriptions [8–12] that can be considered as 'explicitly' or 'implicitly' non-local models due to the presence of internal length parameters and dispersion properties in wave propagation [9,13,14]. In this framework, strain gradient, or non-local models of explicit type [15], have been presented [16–18], as well as models referable to micromorphic continua, in particular, the micropolar continua, that can be considered non-local models of implicit type [19–27].

Communicated by Victor Eremeyev, Holm Altenbach.

V. Settimi · P. Trovalusci (✉) · G. Rega
Dipartimento di Ingegneria Strutturale e Geotecnica, Università degli Studi di Roma La Sapienza, Rome, Italy
E-mail: patrizia.trovalusci@uniroma1.it

Published online: 28 March 2019

Within this latter class of implicit non-local models, moreover, a multiscale approach that can be classified among continua with affine microstructure [8] or continua with configurational forces [10], has been pursued, as presented and described in [28–33]. The method consists in the description of the mechanical behavior of a continuum model, i.e., the macromodel, and of a complex lattice model, representing the micromodel. The field variables at the two material scales are linked via an energy equivalence criterion. The obtained model is characterized by the presence of more field descriptors than the classical continuum, allowing to retain the memory of the fine organization of the material.

The presence of the microstructure plays an important role when the dynamical behavior of these materials is investigated, especially in nowadays applications where high-frequency excitations are commonly used. In fact, when excitation wavelengths are comparable with microstructure length, dispersion effects due to the microstructure reveal the multiscale nature of the material [34,35].

Wave propagation in microstructured solids has been investigated with a great variety of approaches aimed at highlighting the dispersion features due to the presence of heterogeneities. Focusing on the one-dimensional setting of interest herein, models have been formulated based on homogenization [36,37], gradient-type [38–41], generalized continua [42,43], or internal variables theories [44,45], as well as lattice theory [46]. The classical wave equation of linear elastic wave propagation in homogeneous solids has been generalized by considering space, time, and/or mixed fourth-order derivatives of the macrodisplacement, and by introducing a microstructure contribution to slowing down the propagation velocity with respect to the one in the medium without microstructure. An overview of dispersive wave equations has been presented in [47], according to the unified viewpoint of internal variables. Dispersion properties highlighted by different, and possibly simplified, models have been compared, among others, in [34,35,43,48], also paying attention to their capability to reproduce physically realistic behaviors [49].

The present work aims at analytically investigating the dynamical behavior of a multiscale model, in order to critically discuss the influence of the micromodel descriptors on the overall response. Reference is made to a model of mono-dimensional bar of elastic material with distributed stationary microcracks, derived from the generalized continuum formulation in [31,32] and used therein and in [33] for a preliminary numerical investigation of the features of wave propagation. Microcracks are described by a microdisplacement to be added to the standard macrodisplacement. The ensuing, coupled, balance equations give rise to a higher-order dispersion wave equation which includes all fourth-order derivatives of the macrodisplacement variables considered in the literature models and accounting for the zero-order microdisplacement responsible for dispersion phenomena [32], however, with no change of the macroscopic velocity in the linear wave operator due to the presence of the microstructure [47]. Such higher-order dispersion wave equation, to the best of our knowledge, appears to have been not yet used in the literature for an extensive investigation of the dispersion properties of a physically based microcracked bar model aimed at determining the overall response, by also accounting for the influence of the internal parameters which describe cracks density and length. Indeed, the modification of these parameters entails description of bars under different levels of damage, and proves to be able to meaningfully alter shape, velocity, and actual occurrence of propagating waves, with also significant distorting effects of the macrodisplacement response, especially due to coupling.

The paper is organized as follows. A brief description of the reference model for the microcracked bar is presented in Sect. 2, while wave propagation is addressed in Sect. 3 in analytical terms. The influence of the coupling between macro- and microdescriptors and of the damage parameters on the system dynamical behavior is discussed in Sects. 3.1 and 3.2. As a real example, the response of a harmonically excited long bar is described in Sect. 4, and some final comments are summarized in Sect. 5.

2 Multiscale–multifield model: one-dimensional microcracked bar

The reference system is a microcracked bar characterized by a uniform distribution of fibers and cracks, whose formulation is derived from the generalized formulation presented in [32], relevant to a multifield continuum with affine microstructure [8] as well as a continuum with configurational forces [10]. Moving from the 2D model, whose representative volume is sketched in Fig. 1a, to the mono-dimensional domain shown in Fig. 1b, the bar is described by two interacting lattice systems, one being the fibers in the matrix represented by a lattice of rigid particles, the other representing microcracks, modeled as interacting deformable slits with dominant dimension, localized in between the particles. The two lattices are linked together by nonlinear elastic bonds. For the sake of simplicity, the fibers are considered ‘frozen’ in such a way that the microrotation and the work-conjugated microcouple are null [14].

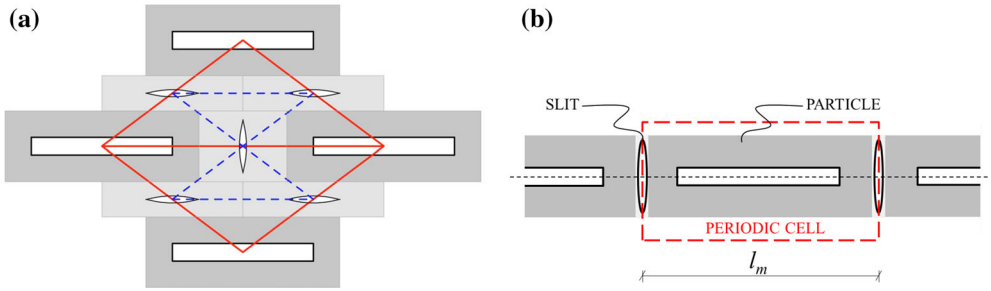

Fig. 1 2D orthotropic module with particles and slits (**a**) and corresponding mono-dimensional model with identification of the periodic cell (**b**)

The constitutive equations of the multifield continuum are directly derived from a proper micromechanical description via energy equivalence [31,32]. Following the homogenization formulation presented in [33], to refer to for all details, and under the above-mentioned assumption of 'frozen' fibers, the linearized stress–strain relationships in the one-dimensional framework read [14]:

$$\begin{aligned} S &= A\,u_x + D\,d_x \\ z &= M\,d \\ Z &= O\,u_x + R\,d_x, \end{aligned} \tag{1}$$

where u and d represent the macro-, standard, displacement, and the additional microdisplacement, accounting for the presence of the material microstructure, respectively, S is the standard Cauchy stress, while z is the internal volume force and Z the microstress related to the presence of the microcracks, the lower suffix indicating the derivation variable. The constitutive constants A, D, O, R, and M are identified as in [32,33]. In particular, for the considered model, the A component is set equal to the axial stiffness YA_s, with Y Young modulus and A_s cross-section area of the bar, $R = nY/\rho_m \pi l_c$ and $M = mY\rho_m/\pi l_c$, where $\rho_m = 1/l_m$ is the linear microcrack density (l_m being the unit module length, Fig. 1b), l_c is the microcrack length, and n and m are constants dependent on the number and arrangement of the microcracks in a representative portion of the material referred as the 'module'. As far as the coupling terms D and O are concerned, the material hyperelasticity entails $O = D$. The identification procedure shows that the coupling term can generally depend on the microcrack size and arrangement and on the elastic constants of the matrix [50]. However, since the present work is aimed at studying the influence of coupling and damage on the system response, the coupling term is assumed to be independent of the damage parameters, in order to clearly distinguish the effects of one and the others. Consequently, in the following, D is assumed to be proportional to the elastic axial stiffness A, i.e., $D = \delta A$, and the coupling parameter δ is given physically reasonable values equal to a low percentage of the elastic stiffness.

Balance equations are derived by imposing the equivalence of the external and internal virtual works, which, in the presence of only inertial actions, leads to:

$$\begin{aligned} u_{tt} - \alpha^2 u_{xx} - \beta d_{xx} &= 0 \\ d_{tt} - \varepsilon u_{xx} - \varphi^2 d_{xx} + \eta d &= 0 \end{aligned} \tag{2}$$

where $\alpha = A/\rho$, $\beta = D/\rho$, $\varepsilon = O/\mu$, $\varphi = R/\mu$ and $\eta = M/\mu$, ρ and μ being the macro- and micromass densities, respectively. All details of the relevant identification are also reported in [32]. Due to the hypothesis of material hyperelasticity ($D = O$) and to the assumed form for the coupling term ($D = \delta A$), the $\alpha, \beta, \varepsilon$ parameters of Eq. (2) are not independent of each other, holding the following relations: $\beta = \delta\alpha = \varepsilon\mu/\rho$.

It is worth noting that Eq. (2), which ensues from the generalized 3D continuum formulation of [32], accounts for the one-dimensional coupling between macromotion and micromotion via the correspondingly exchanged second-order derivatives d_{xx} and u_{xx}. Thus, in the case $\beta = \varepsilon$ considered in the following, the present model corresponds to the microstructure model II presented in the review article [47], in the framework of the description of the microstructural effects in 1D continua in terms of internal variables. The fourth-order space derivative of macromotion appearing in the associated higher-order dispersion wave equation

$$u_{tt} = \alpha^2 u_{xx} + \frac{\varphi^2}{\eta}\left(u_{tt} - \alpha^2 u_{xx}\right)_{xx} - \frac{1}{\eta}\left(u_{tt} - \alpha^2 u_{xx}\right)_{tt} + \frac{\beta^2}{\eta} u_{xxxx} \tag{3}$$

does not entail the slowing down of the wave propagation velocity due to coupling which is instead exhibited by the second-order space derivative occurring in the same equation of the microstructure model I [see Eq. (88) of [47]]. The latter represents the general model of dispersive wave propagation based on the Mindlin theory of microstructure [51] proposed in [43]. Although wave dispersion has recently been addressed also with a somehow richer model in the internal variable perspective (e.g., the unified model in [35]), the latter is the one more widely considered in the literature for analyzing dispersion curves and the corresponding wave profiles [34,43]. It is thus worth analyzing the dynamical properties of the microcracked bar as ensuing from the present alternative modeling of coupling, in which dispersion effects are only due to the whole set of fourth-order derivatives entering the wave equation, with no change of macroscopic velocity due to the microstructure occurring in the linear wave operator.

When analyzing the dynamical properties of the bar, attention is devoted to critically investigate the effects of the microcracks represented by the microcrack density, ρ_m, and microcrack length, l_c, respectively. Moreover, the influence of the coupling in the model response is also studied by means of the coupling parameter δ.

3 Wave propagation

To analytically study the free wave propagation inside the microcracked bar, a general harmonic form for both macro-, u, and micro-, d, displacements is assumed:

$$\begin{aligned} u &= u_0\, \mathrm{e}^{ikx}\mathrm{e}^{-i\omega t} \\ d &= d_0\, \mathrm{e}^{ikx}\mathrm{e}^{-i\omega t} \end{aligned} \tag{4}$$

as a function of the spatial and temporal variables x and t, respectively. The harmonic waves are characterized by wave number k and angular frequency ω, while u_0 and d_0 are the oscillation amplitudes which are assumed to be constant. Substitution of (4) into (2) allows us to rewrite the system as follows:

$$(\mathbf{A} - \omega^2 \mathbf{I})\, \mathbf{v} = 0 \tag{5}$$

where $\mathbf{I}$ is the identity tensor and the components of the vector $\mathbf{v}$ and the tensor $\mathbf{A}$ are:

$$\{\mathbf{v}\} = \{u \quad d\}^T, \qquad [A] = \begin{bmatrix} k^2\alpha^2 & k^2\beta \\ k^2\varepsilon & \eta + k^2\varphi^2 \end{bmatrix} \tag{6}$$

Solving the system characteristic equation

$$k^4(\alpha^2\varphi^2 - \beta\varepsilon) + k^2(\alpha^2\eta - (\alpha^2 + \varphi^2)\omega^2) - \eta\omega^2 + \omega^4 = 0 \tag{7}$$

leads to the expressions for the wavenumbers k_i:

$$k_{1,2,3,4}(\omega) = \pm\sqrt{\frac{-\varphi^2\omega^2 + \alpha^2(\eta - \omega^2) \pm \sqrt{4(\beta\varepsilon - \alpha^2\varphi^2)\omega^2(-\eta + \omega^2) + (\alpha^2\eta - (\alpha^2 + \varphi^2)\omega^2)^2}}{2\beta\varepsilon - 2\alpha^2\varphi^2}} \tag{8}$$

and, by recalling the definition of phase velocity $c = \omega/k$,

$$c_{1,2,3,4}(k) = \pm\sqrt{\frac{\alpha^2 + \frac{\eta}{k^2} + \varphi^2 \pm \frac{\sqrt{\eta^2 + 2k^2\eta(\varphi^2 - \alpha^2) + k^4(4\beta\varepsilon + (\alpha^2 - \varphi^2)^2)}}{k^2}}{2}} \tag{9}$$

Obviously, $k_1 = -k_2$ ($c_1 = -c_2$) and $k_3 = -k_4$ ($c_3 = -c_4$) so that only two wavenumbers and phase velocities are considered.

The spatial form of micro- and macrodisplacements is thus determined by the superposition of two harmonic contributions governed by real k_1 and k_3 wavenumbers, as follows:

$$\begin{aligned} u(x) &= u_1(x) + u_3(x) \\ d(x) &= d_1(x) + d_3(x) \end{aligned} \tag{10}$$

where

$$\begin{aligned} u_1(x) &= \phi_{1u}\left(\frac{1}{2}C_1 e^{ik_1 x} + \frac{1}{2}\bar{C}_1 e^{-ik_1 x}\right) \\ u_3(x) &= \phi_{3u}\left(\frac{1}{2}C_3 e^{ik_3 x} + \frac{1}{2}\bar{C}_3 e^{-ik_3 x}\right) \\ d_1(x) &= \phi_{1d}\left(\frac{1}{2}C_1 e^{ik_1 x} + \frac{1}{2}\bar{C}_1 e^{-ik_1 x}\right) \\ d_3(x) &= \phi_{3d}\left(\frac{1}{2}C_3 e^{ik_3 x} + \frac{1}{2}\bar{C}_3 e^{-ik_3 x}\right) \end{aligned} \tag{11}$$

C_1, C_3 (and the relevant complex conjugate $\bar{C}_1$, $\bar{C}_3$) are unknown amplitudes to be determined by solving the boundary condition problem, and $\{\phi_{1u}, \phi_{1d}\}$ and $\{\phi_{3u}, \phi_{3d}\}$ are the components of the two eigenvectors $\boldsymbol{\phi_1}$ and $\boldsymbol{\phi_3}$ associated with k_1 and k_3, respectively. Their expression is:

$$\boldsymbol{\phi_{1,3}} = \left\{ \frac{-\alpha^2\eta + \alpha^2\omega^2 - \varphi^2\omega^2 \pm \sqrt{4(\beta\varepsilon - \alpha^2\varphi^2)\omega^2(-\eta + \omega^2) + (\alpha^2\eta - (\alpha^2 + \varphi^2)\omega^2)^2}}{2\varepsilon\omega^2}, 1 \right\} \tag{12}$$

In the following analyses, eigenvectors are normalized as follows: $\bar{\boldsymbol{\phi}}_{\mathbf{1}} = \{\phi_{1u}, \phi_{1,d}\}/\sqrt{\phi_{1u}^2 + \phi_{1d}^2}$ and $\bar{\boldsymbol{\phi}}_{\mathbf{3}} = \{\phi_{3u}, \phi_{3,d}\}/\sqrt{\phi_{3u}^2 + \phi_{3d}^2}$.

It is worth briefly investigating the response of the lattice model when no interactions between particles and microcracks are taken into account. This corresponds to solve the uncoupled system, obtained when $\beta = \varepsilon = 0$ in (2), where the macromotion u corresponds to the standard wave equation while the micromotion d remains dispersive. The relevant wavenumbers of the macro- and microdisplacements read:

$$k_u(\omega) = \frac{\omega}{\alpha}, \qquad k_d(\omega) = \frac{\sqrt{\omega^2 - \eta}}{\varphi} \tag{13}$$

while the phase velocities are:

$$c_u = \alpha, \qquad c_d = \sqrt{\varphi^2 + \frac{\eta}{k^2}} \tag{14}$$

To discuss the influence of coupling and damage parameters on the dynamical behavior of the proposed model, the results presented in the next sections are nondimensionalized with respect to the length of a single periodic cell (Fig. 1b). Since, in the mono-dimensional bar, the microcracks are assumed to be orthogonal to the bar axis, the cell length is determined by the microcrack density ρ_m through the following relation: $l_m = 1/\rho_m$. Accordingly, the nondimensional wavenumber reads $\bar{k} = k\, l_m$.

The following numerical analyses are referred to a concrete bar ($Y = 31.5 \cdot 10^6$ kN/m^2) of cross-section area $A_s = 10^{-2}$ m^2, for which $m = 1, \quad n = 0.8, \quad \mu = 1, \quad \rho = 1$.

3.1 Influence of the coupling terms

Starting from the limiting case of uncoupled system, that corresponds to neglect the link between the fibers and microcracks, the effect of increasing coupling between macro- and microdisplacements is analyzed in terms of propagation frequency and velocity in Fig. 3. Looking at the response of the uncoupled system (black lines in Fig. 2), the results show the presence of two separated branches, relevant to macro- (ω_u, c_u) and microdisplacements (ω_d, c_d), crossing themselves at a specific (nondimensional) wavenumber value $\bar{k}_{\text{cross}}$, determined by equating Eq. (13) expressed as a function of k (i.e., $\omega_u(k)$, $\omega_d(k)$).

$$\bar{k}_{\text{cross}} = \sqrt{\frac{\rho\, m}{l_c\, \pi\, \mu\, \rho_m - \rho\, n}} \tag{15}$$

Evolution of phase velocities in Fig. 2a shows the presence of two branches, the upper branch $c_u = c_0 = \alpha$ and the lower branch c_d, the latter being characterized by a dispersive behavior, i.e., the dependence of the

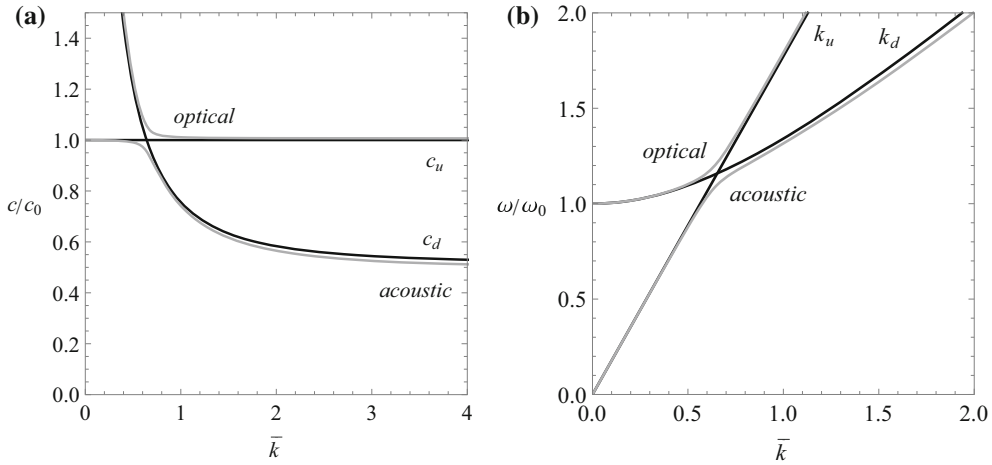

Fig. 2 Phase velocities (a) and frequency spectra (b) for the uncoupled system (black lines) and for the coupled system (gray lines) with $\rho_m = 100\ \mathrm{m}^{-1}$ and $l_c = 0.01$ m

propagation velocity on the wavenumber, for low values of the nondimensional wavenumber ($\bar{k} < 4.5$). For higher wavenumbers, both branches become independent of velocity.

As regards the frequency spectra of Fig. 2b, it is possible to identify the cutoff frequency ω_0, which corresponds to the frequency value of the dispersive curve at $k = 0$, where the spatial variation of the micromotion is null. The cutoff frequency marks the lower frequency boundary for microwave propagation; in fact, relevant wavenumbers for frequencies $\omega < \omega_0$ are imaginary, and the corresponding wave is hyperbolic ($\cosh(kx)$). As a consequence, only standing microwaves exist and wave propagation is possible only for the macromotion for frequencies lower than the cutoff frequency. Its expression in terms of physical parameters of the system is

$$\omega_0 = \sqrt{\frac{Y\ m\ \rho_m}{\mu\ l_c\ \pi}} \tag{16}$$

It can be observed that the cutoff frequency depends on both the damage parameters ρ_m and l_c, but it is independent of the coupling parameter δ.

Moving from this scenario, the presence of coupling terms prevents the curves from crossing and induces the veering phenomenon, as highlighted by the gray lines in Fig. 2. Around the crossing point, the two frequency (and velocity) curves approach each other and then veer away due to the coupling, with the veering region which enlarges for increasingly coupled systems, as shown in the enlargements of Fig. 3. So-called acoustic (optical) curves, corresponding to waves with vanishing (non-vanishing) frequency when the wavenumber $\bar{k}$ is vanishing [52], are identified.

The effect of veering in the wave form of the system response is analyzed in Figs. 4 and 5. As shown in Eqs. (10), (11), the spatial form of both micro- and macrodisplacements is defined as linear combination of two harmonic waves depending on k_1 (optical) and k_3 (acoustic) wavenumbers, respectively, whose evolution is reported in Fig. 4a. At equal amplitudes (C_1, C_3, still unknown), the relative influence of each harmonic wave on the micro- and macrodisplacement is governed by the (normalized) eigenvectors $\boldsymbol{\phi_1}$ and $\boldsymbol{\phi_3}$, which strongly vary around the veering region, as shown in Fig. 4b. It is thus possible to verify the response components before and after the veering region (Fig. 5), preliminarily observing that the harmonic contributions to the macro- and micromotion governed by k_1 and k_3 are in-phase and out-of-phase, respectively.

At about the cutoff frequency ($\omega \approx \omega_0$), the k_1 wave is associated only with the microdisplacement d, while the k_3 wave dominates the u response (Fig. 5a). Conversely, at high frequencies (Fig. 5e), the microdisplacement d is essentially governed by the k_3 wave, with the k_1 wave dominating the u response. When approaching the frequency veering region from below, Fig. 5b (above, Fig. 5d), the k_3 (k_1) waves switch their role, with the two exchanges occurring at mirrored frequency values and the two harmonic contributions of the microdisplacement becoming dominant. At the former crossing frequency ($\omega_u/\omega_0 = \omega_d/\omega_0 = 1.16$, Fig. 5c), the distribution of the k_1 and k_3 components on the two displacements is identical, however, with a marked dominance of those associated with the microdisplacement d. Thus, the presence of the veering entails a meaningful reduction in both the k_3 and k_1 contributions of the macrodisplacement, with a transfer of energy to the corresponding

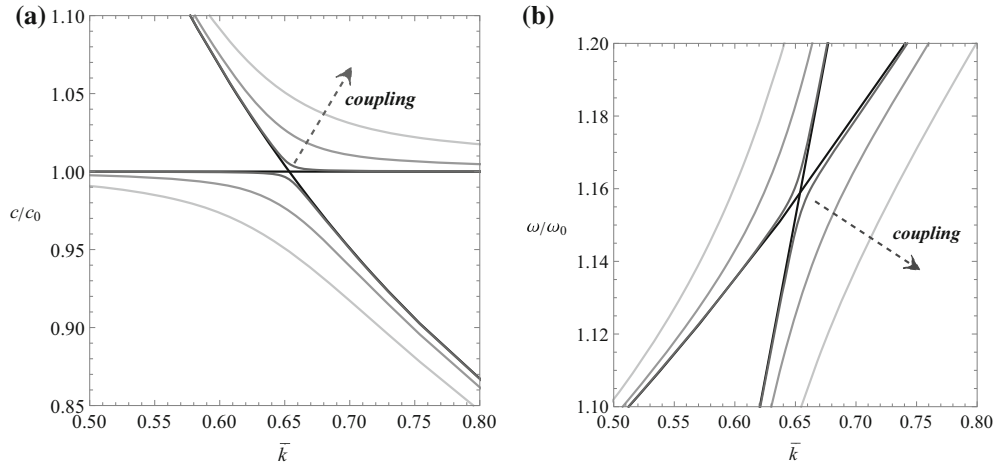

Fig. 3 Phase velocities (**a**) and frequency spectra (**b**) for $\delta = 0.0$ (i.e., uncoupled system, black), $\delta = 0.01$ (dark gray), $\delta = 0.05$ (gray) and $\delta = 0.1$ (light gray), with $\rho_m = 100\ \mathrm{m}^{-1}$ and $l_c = 0.01$ m

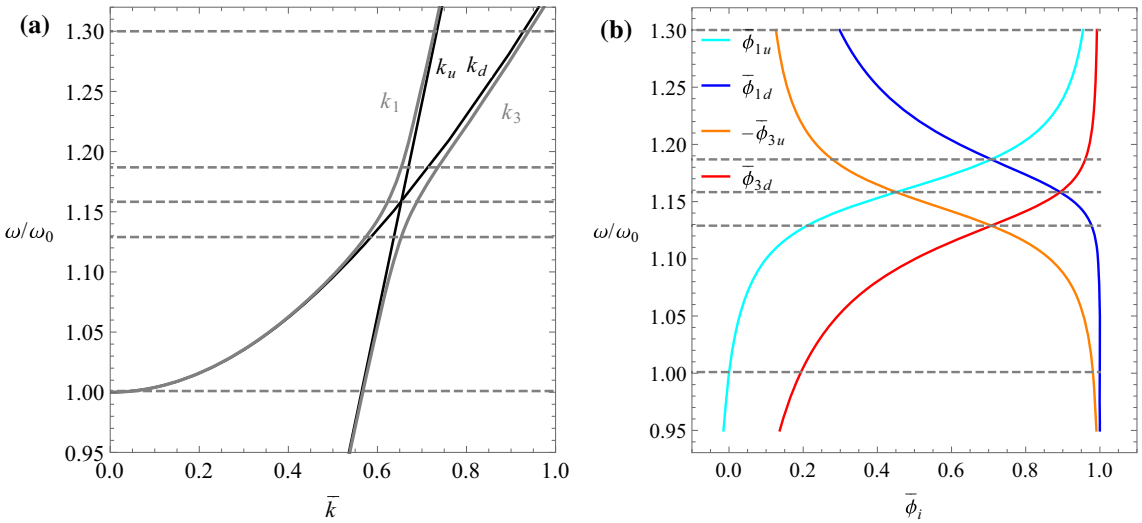

Fig. 4 Frequency spectra of the uncoupled (black) and coupled system (**a**); behavior of the eigenvectors components $\bar{\phi}_{1u}$ (cyan), $\bar{\phi}_{1d}$ (blue), $\bar{\phi}_{3u}$ (orange), $\bar{\phi}_{3d}$ (red) (**b**), for $\delta = 0.05$, $\rho_m = 100\ \mathrm{m}^{-1}$ and $l_c = 0.05$ m (color figure online)

ones of the microdisplacement and an ensuing hybridization of the overall response (see Sect. 4 forward). As a consequence of the strong interaction between the waves, a rapid and evident change in the group velocity of the propagating waves can be observed in the veering region, as reported in Fig. 6.

Looking at the response of the uncoupled system (Fig. 6a), the dispersion effect can be recognized in the behavior of the velocities of the acoustic branch, for which the acoustic phase velocity curve gradually approaches from above the asymptotic value, while the group velocity branch initially assumes evidently lower values, and then slowly increases reaching the same regime of the relevant phase velocity curve. When coupling is added to the model (Fig. 6b), the switching phenomenon causes the involvement of also the optical branch, and around the veering region the swift exchange of roles of the two curves marks a clear difference between the corresponding phase and group velocities.

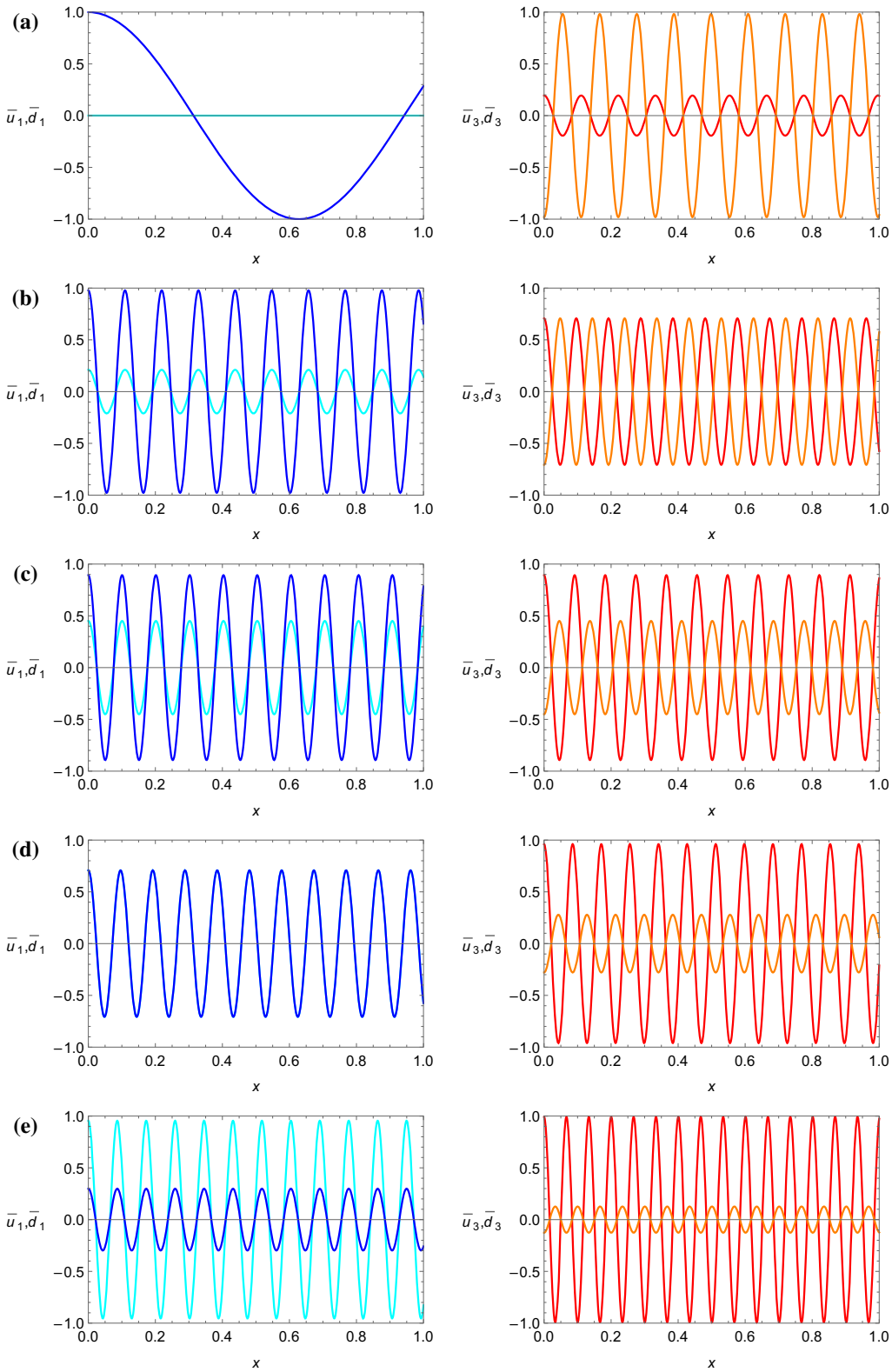

Fig. 5 Harmonic components of the macro- u and micro- d displacements at $\omega/\omega_0 = 1.001$ (**a**), $\omega/\omega_0 = 1.13$ (**b**), $\omega(k_{cross})/\omega_0 = 1.16$ (**c**), $\omega/\omega_0 = 1.19$ (**d**) and $\omega/\omega_0 = 1.3$ (**e**), at $\delta = 0.05$, $\rho_m = 100$ m^{-1} and $l_c = 0.01$ m. Cyan curve: $\bar{u}_1(x)$, blue curve: $\bar{d}_1(x)$, orange curve: $\bar{u}_3(x)$, red curve: $\bar{d}_3(x)$ (color figure online)

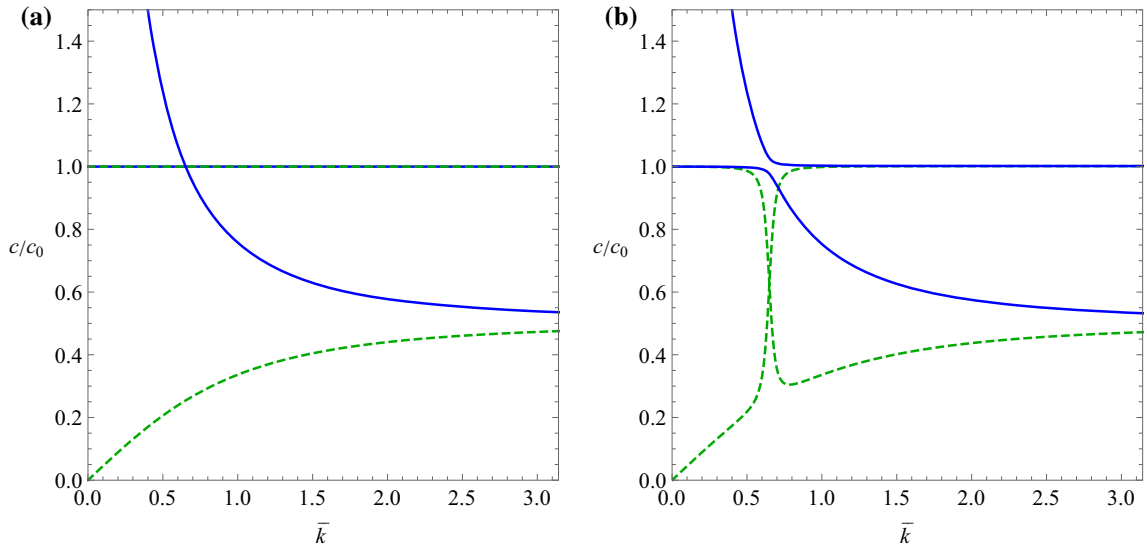

Fig. 6 Comparison between phase velocity (blue) and group velocity (dashed green) for the uncoupled system ($\delta = 0$) (**a**) and for the coupled system ($\delta = 0.05$) (**b**), for $\rho_m = 100\ \mathrm{m}^{-1}$ and $l_c = 0.01$ m (color figure online)

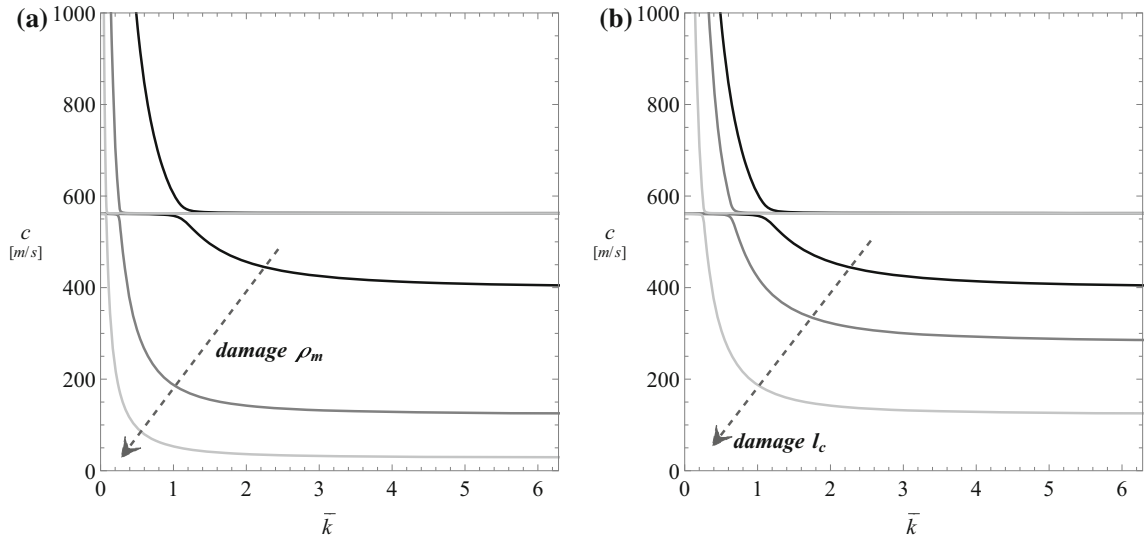

Fig. 7 Phase velocity curves for $\rho_m = 10\ \mathrm{m}^{-1}$ (dark gray), $\rho_m = 100\ \mathrm{m}^{-1}$ (gray) and $\rho_m = 1000\ \mathrm{m}^{-1}$ (light gray), with $l_c = 0.05$ m and $\delta = 0.05$ (**a**); phase velocity curves for $l_c = 0.005$ m (dark gray), $l_c = 0.01$ m (gray) and $l_c = 0.05$ m (light gray), with $\rho_m = 100\ \mathrm{m}^{-1}$ and $\delta = 0.05$ (**b**)

3.2 Influence of the damage parameters

To verify the effects of the microcrack parameters on the free wave propagation, the coupling parameter is set to $\delta = 0.05$ and the dispersion curves in terms of frequency spectra and phase velocities are obtained for different values of the microcrack density ρ_m and of the microcrack length l_c. In particular, three set of values are considered for each parameter, corresponding to low damaged ($\rho_m = 10\ \mathrm{m}^{-1}$), medium damaged ($\rho_m = 100\ \mathrm{m}^{-1}$) and high damaged ($\rho_m = 1000\ \mathrm{m}^{-1}$) bar, with short ($l_c = 0.005$ m), medium ($l_c = 0.01$ m) and long ($l_c = 0.05$ m) microcracks.

In Fig. 7 the effects of ρ_m and l_c parameters on the phase velocities are reported, highlighting, as confirmed by the experience, that damage causes a sensible reduction of the acoustic velocity. Moreover, it can be noted that the cross-point is moved to lower nondimensional wavenumbers as the damage increases, and the relevant veering region is reduced. While producing the same effect with respect to the phase velocities, the

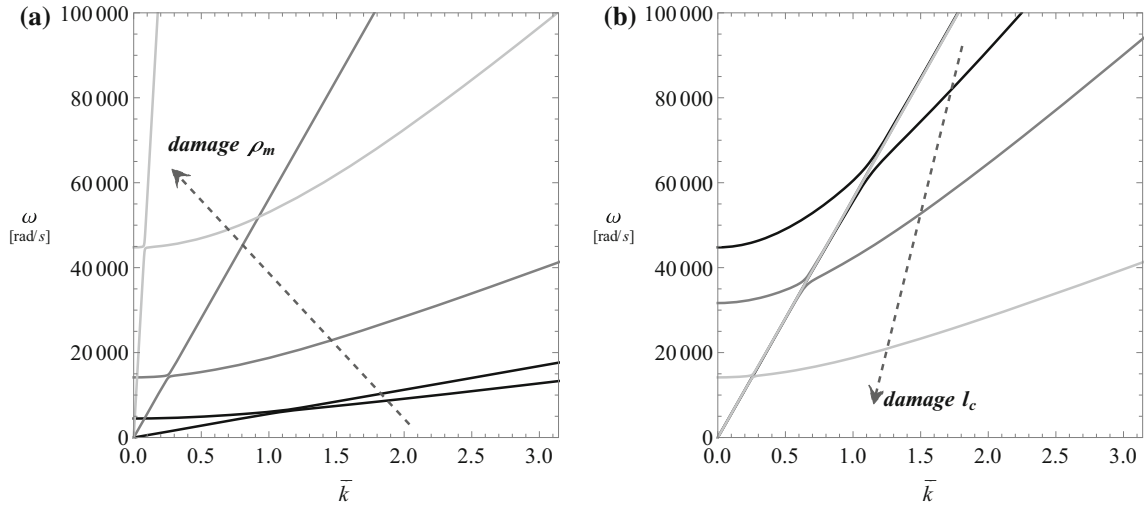

Fig. 8 Frequency spectra for $\rho_m = 10$ m^{-1} (dark gray), $\rho_m = 100$ m^{-1} (gray) and $\rho_m = 1000$ m^{-1} (light gray), with $l_c = 0.05$ m and $\delta = 0.05$ (**a**); frequency spectra for $l_c = 0.005$ m (dark gray), $l_c = 0.01$ m (gray) and $l_c = 0.05$ m (light gray), with $\rho_m = 100$ m^{-1} and $\delta = 0.05$ (**b**)

two parameters have slightly different consequences on the frequency spectra, as shown in Fig. 8. In fact, the microcrack density is responsible for an increase in the cutoff frequency ω_0 (Fig. 8a), while the microcrack length reduces it, thus widening the range of propagation (Fig. 8b). Such different behavior is likely due to the choice to consider vertical microcracks, whose length l_c does not modify the cell dimension, that is governed by the microcrack density ρ_m. Considering horizontal microcrack would likely imply a different influence of their length on the behavior of the frequency spectra. The presented results are also confirmed by the analytical expressions (15) and (16), where it is evident the same (inverse) role played by ρ_m and l_c parameters on the cross-point (cutoff frequency) occurrence. It is interesting to note that the microcrack density affects the behavior of both frequency curves, for the coupled and the uncoupled system, as well. Indeed, the results discussed in this section can be entirely extended to the system with $\delta = 0$, apart from considerations on the veering region which disappears in the latter case. This allows us to assert that the damage parameters are able to concurrently modify the micro- and the macrodisplacements even when they are not coupled. However, Eqs. (13)–(14) prove the independence of k_u and c_u with respect to ρ_m and l_c parameters. This apparent inconsistency can be explained by remembering that the presented results are nondimensionalized with respect to the periodic cell length, which is inversely proportional to the microcrack density. Consequently, the three curves in Fig. 8a are actually relevant to three different space domains, which reduce as the damage increases, and the frequency curve of the macrodisplacement (the straight curve of Fig. 2a for the uncoupled system) is scaled to the cell dimension too. It entails that a change in the scaling length (i.e., a change in the ρ_m value) causes a modification of the macroresponse even if it is independent of the damage.

The outcomes are summarized in the behavior charts of Fig. 9, where the concomitant effect of the two damage parameters can be easily read. The microcrack length strongly modifies the nondimensional cross-wavenumber and the dimensional cutoff frequency, especially in the short length range, between 0 and 0.02 m. For higher values, the influence of l_c is less evident, as somehow expected, being the presence (and not the length) of the vertical microcrack the actual source of damage. As concerns the microcrack density, the strongest effect is relevant to the cross-point $\bar{k}_{\text{cross}}$ position, which obviously indicates also the location of the veering region, reported in Fig. 9a. Here, an increase in an order of magnitude of ρ_m (from 10 to 100 m^{-1}) implies a dramatic decrease in the wavenumber associated with $\bar{k}_{\text{cross}}$, while its effect is less intense in increasing the cutoff frequency ω_0 (Fig. 9b).

Focusing on strongly coupled and highly damaged models, it can be observed that one of the frequency or velocity curves can possibly fall to zero, as shown in Fig. 10. The critical value $\bar{k}_{\text{lim}}$ of the nondimensional wavenumber corresponding to zero velocity is determined by the following analytical expression:

$$\bar{k}_{\text{lim}} = \frac{\sqrt{m}}{\sqrt{-n + l_c\ \pi\ \delta^2\ \rho_m}} \tag{17}$$

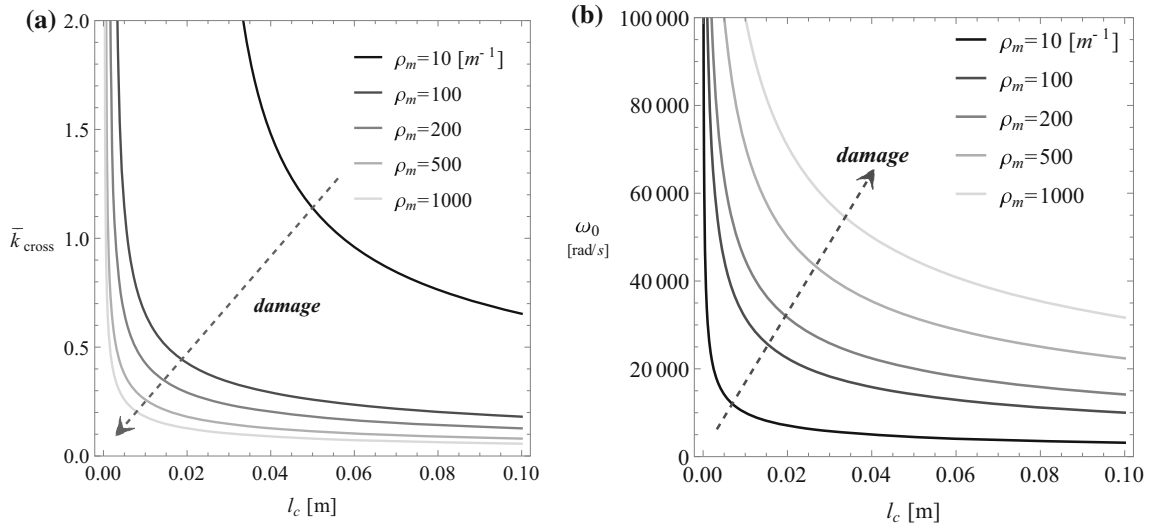

Fig. 9 Effect of damage parameters on the nondimensional value of the cross-wavenumber and on the dimensional value of the cutoff frequency: behavior chart in the l_c–$\bar{k}_{\text{cross}}$ plane (**a**) and in the l_c–ω_0 plane (**b**)

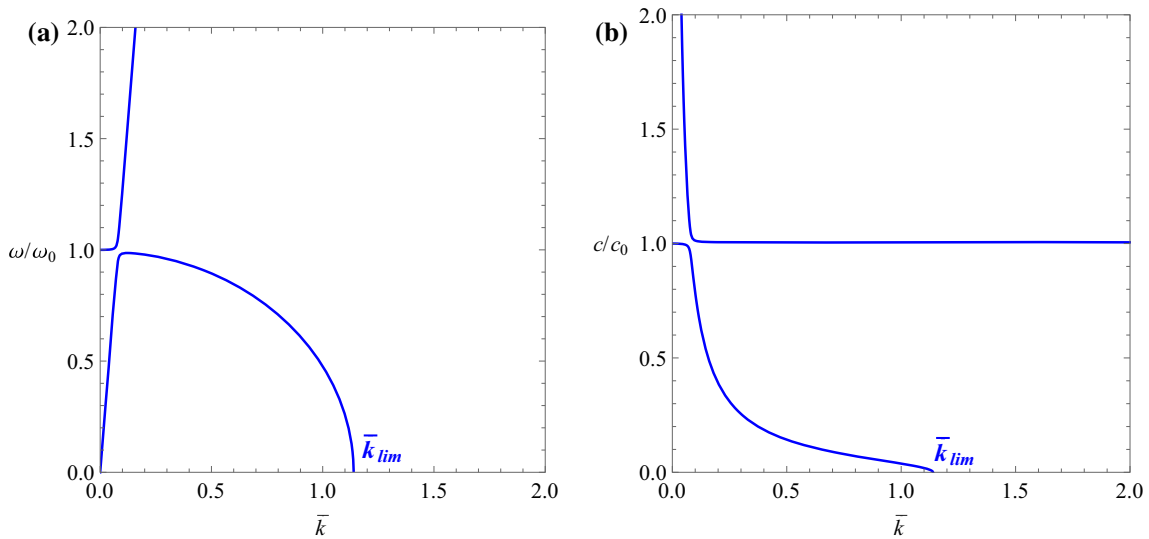

Fig. 10 Frequency spectra (**a**) and phase velocity curves (**b**) for $\rho_m = 1000\ \text{m}^{-1}$, $l_c = 0.05$ m and $\delta = 0.1$

The point marks a qualitative change in the response of the model. In fact, for $\bar{k} > \bar{k}_{\text{lim}}$ no acoustic curve can be detected and corresponding wave propagation is precluded. From Eq. (17), it follows that the critical wavenumber depends on all the control parameters, so that their combined effect is investigated by means of the behavior charts of Fig. 11. Both charts highlight the major role played by the coupling in determining the $\bar{k}_{\text{lim}}$ occurrence, which is possible, for reasonable values of the physical parameters, only in the strongly coupled regime.

Focusing on the damage parameters, the critical value of the microcrack density responsible for the occurrence of $\bar{k}_{\text{lim}}$ can be analytically identified:

$$\rho_{m,\text{lim}} = \frac{n}{l_c\ \pi\ \delta^2} \tag{18}$$

The effects of positive and negative variations of the microcrack density with respect to $\rho_{m,\text{lim}}$ on the frequency spectra are reported in Fig. 12. As already commented, for $\rho_m < \rho_{m,\text{lim}}$ (Fig. 12b) the cutoff frequency ω_0 identifies two frequency regions corresponding to different space forms of the propagating wave,

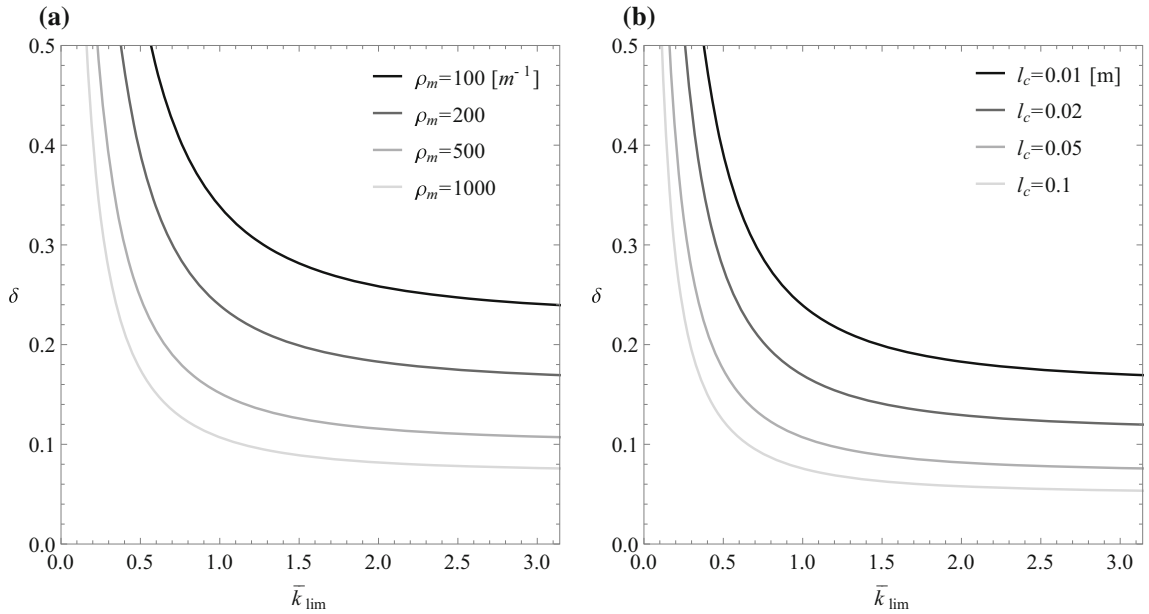

Fig. 11 Behavior charts in the $\bar{k}_{\lim}$–δ plane for varying values of the microcrack density ρ_m, with $l_c = 0.05$ m (**a**) and of the microcrack length l_c, with $\rho_m = 1000$ m^{-1} (**b**)

i.e., the sole acoustic k_3 component for $\omega < \omega_0$ and the superposition of k_1 and k_3 harmonic waves described by Eqs. (10) and (11) when $\omega > \omega_0$ and both optical and acoustic branches have real wavenumbers. For increased damaged models, if $\rho_m > \rho_{m,\lim}$, the acoustic branch falls to zero and a band gap (gray region in Fig. 12c) arises for frequencies belonging to the ω_0–ω_{up} range, where the ω_{up} value is achievable by zeroing the derivative of $\omega(k)$ with respect to k, and then calculating the relevant frequency value. The result reads

$$\omega_{\text{up}} = \sqrt{\frac{\eta - \sqrt{\frac{\beta\varepsilon\eta^2}{\beta\varepsilon-\alpha^2\varphi^2}} + \frac{\alpha^2\eta^2\varphi^2(\alpha^2+\varphi^2)}{\alpha^4\eta\varphi^2+\beta\varepsilon\eta\varphi^2+\sqrt{\beta\varepsilon\eta^2(\alpha^2+\varphi^2)^2(\beta\varepsilon-\alpha^2\varphi^2)}-\alpha^2\eta(\beta\varepsilon+\varphi^4)}}{2}} \tag{19}$$

Inside the band gap, both k_1 and k_3 wavenumbers are imaginary and the resulting standing waves oscillate in a confined region of space without propagation [46,52]. Conversely, for frequencies higher than the cutoff one, the sole optical wave governs the spatial form of the micro- and macrodisplacements, and for $\omega < \omega_{\text{up}}$ the acoustic curve furnishes two different wavenumbers to be superimposed in order to define the resulting propagating waves.

4 Forced waves: long bar with harmonic excitation of the free end

The spatial forms of the micro- and macrodisplacements (10) are defined as a function of the unknown C_1 and C_3 amplitudes, to be determined by imposing the boundary conditions at the ends of the bar. To this aim, a model of long bar with harmonic axial force $F(t) = F_0\, e^{i\Omega t}$ applied to one end (at $x = 0$) is investigated. In general, traction on a microcracked bar produces crack-opening displacements, which can be modeled as an applied microforce to be added to the standard macroboundary condition, to obtain:

$$S(0,t) = F(t)/A_s, \quad Z(0,t) = \lambda F(t)/A_s \tag{20}$$

where λ represents the ratio between micro- and macroboundary conditions [32]. To identify the microforce, an energetic equivalence between a damaged bar, simulated by a finite number of longitudinal discontinuities, and an elastic bar with an additional force is developed: $A_s Z = \lambda F(0,t)$, with $\lambda \geqslant 0$. The λ parameter is assumed to depend on the microstructure parameters, i.e., the crack density ρ_m and the crack length l_c, and it is obtained by linking the axial microforce $A_s Z$ to the overall axial displacement of the discontinuities of the

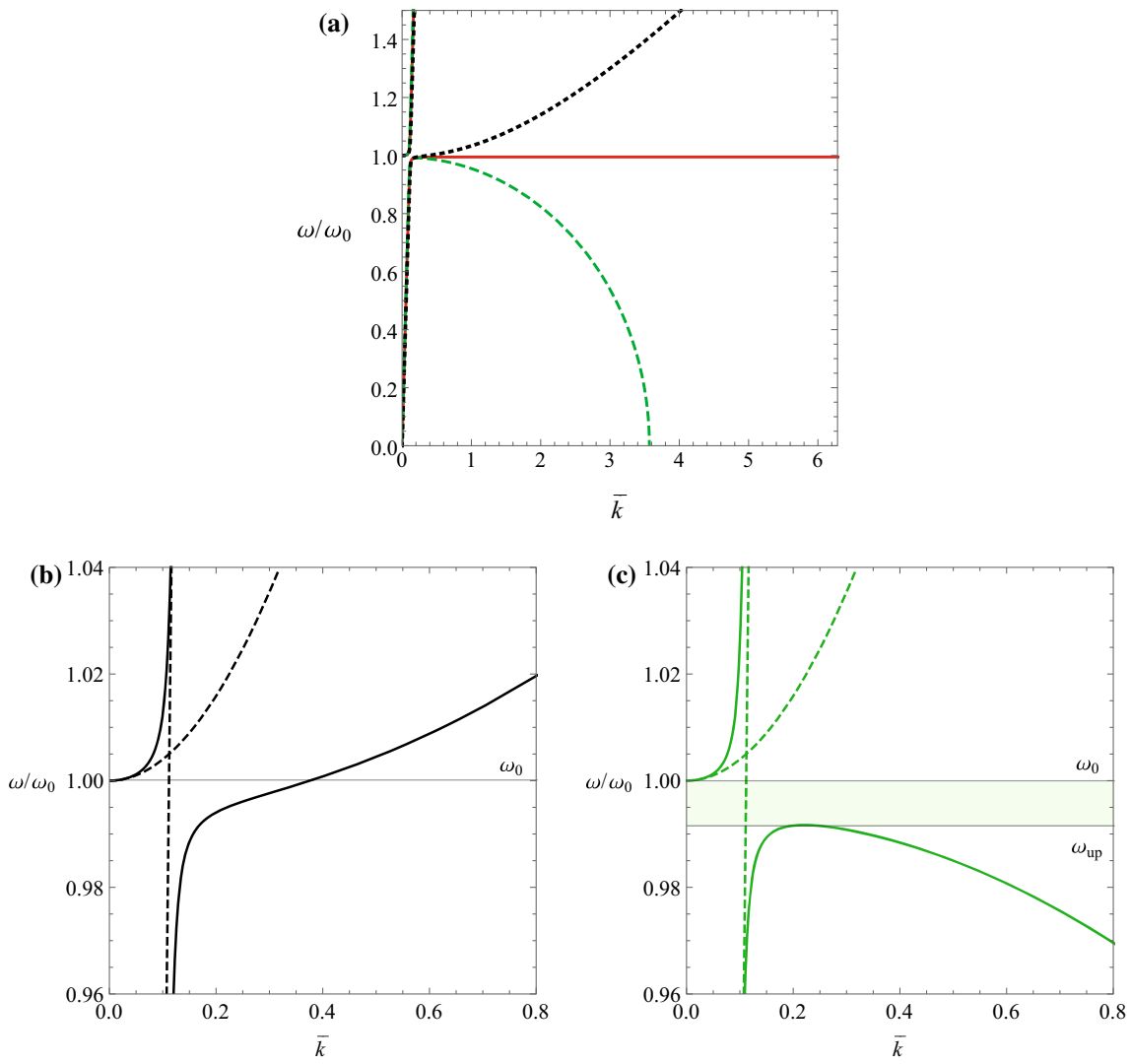

Fig. 12 For $l_c = 0.05$ m and $\delta = 0.1$, frequency spectra for $\rho_m = \rho_{m,\text{lim}}$ (continuous red), $\rho_m < \rho_{m,\text{lim}}$ (dotted black) and $\rho_m > \rho_{m,\text{lim}}$ (dashed green) (**a**); identification of the wave propagation region for the system with $\rho_m < \rho_{m,\text{lim}}$ (**b**) and with $\rho_m > \rho_{m,\text{lim}}$ (**c**), where dashed curves denote the uncoupled case (color figure online)

bar, each contribution being evaluated as the opening displacement of a microcrack in an elastic string with tension at infinity. It follows that $\lambda = \rho_m l_c \pi/2$.

Based on the stress–strain relationships (1), the boundary conditions at $x = 0$ Eq. (20) can be rewritten in terms of the micro- and macrodisplacements, as:

$$u'(0,t) = g_u e^{i\Omega t}, \quad d'(0,t) = g_d e^{i\Omega t}, \tag{21}$$

where

$$g_u = \frac{F_0(n - l_c\pi\delta\lambda\rho_m)}{A_s^2 Y(n - l_c\pi\delta^2\rho_m)}, \quad g_d = \frac{F_0 l_c\pi(\delta - \lambda)\rho_m}{A_s^2 Y(l_c\pi\delta^2\rho_m - n)} \tag{22}$$

Due to the linearity of the problem, it can be deduced that the temporal form of the system response has the same frequency of the forcing term, i.e., $e^{i\Omega t}$. The long bar under analysis can be modeled as a semi-infinite body, so that the boundary condition at infinity imposes that only progressive (rightward) waves have to be considered. Solving the boundary problem allows us to obtain the expressions for C_1 and C_3 amplitudes:

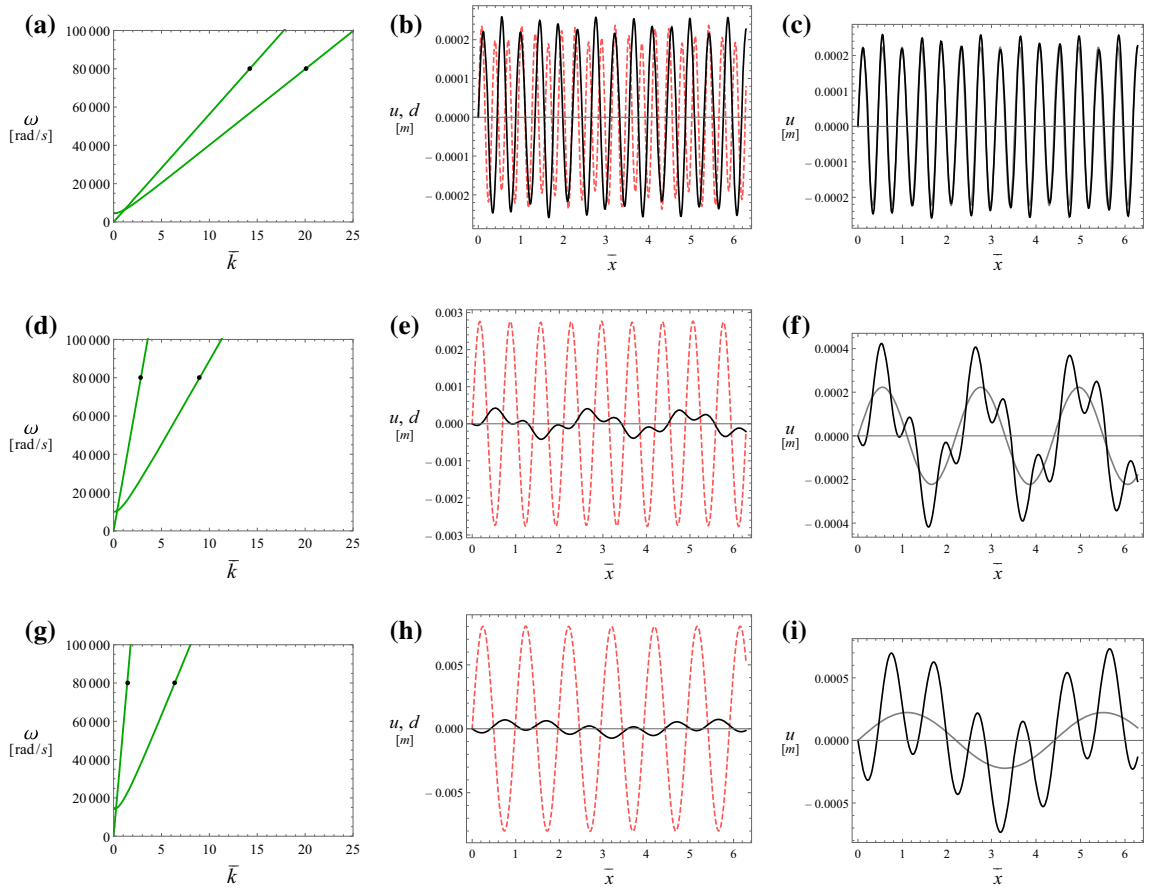

Fig. 13 Frequency spectra and micro- and macrodisplacements for $\rho_m = 10$ m^{-1}(**a**)–(**c**), $\rho_m = 50$ m^{-1}(**d**)–(**f**), $\rho_m = 100$ m^{-1}(**g**)–(**i**). Black waves: macrodisplacement u of the damaged system; dashed red waves: microdisplacement d; gray waves: macrodisplacement u of the undamaged system. $\delta = 0.05$, $l_c = 0.05$ m (color figure online)

$$C_1 = \frac{i(g_u\phi_{3d} - g_d\phi_{3u})}{2k_1(\phi_{1u}\phi_{3d} - \phi_{1d}\phi_{3u})}$$
$$C_3 = \frac{i(g_d\phi_{1u} - g_u\phi_{1d}}{2k_3(\phi_{1u}\phi_{3d} - \phi_{1d}\phi_{3u})} \tag{23}$$

while the relevant complex conjugates are $\bar{C}_1 = iC_1$ and $\bar{C}_3 = iC_3$.

Numerical results are obtained for an increasingly damaged bar subjected to an harmonic excitation of amplitude $F_0 = 100$ kN and frequency $\Omega = 80000$ rad/s, with $\delta = 0.05$ and $l_c = 0.05$ m.

Figure 13 points out the ability of the multifield model to modify the shape of the resulting wave propagating along the bar due to damage. The comparison between undamaged and damaged bar for increasing microcrack density ρ_m is reported in the right-hand panels of Fig. 13. Here the macrodisplacement u is seen to undergo an increasingly evident distortion due to coupling with the microdisplacement d. To interpret the numerical outcomes, it is worth highlighting that the graphics of Fig. 13 represent the wave spatial evolution in relation to the length of the periodic cell, which reduces as the microcrack density increases. As a consequence, the micro- and macrodisplacements refer to a progressively reducing domain moving from the upper to the lower line of Fig. 13. This aspect explains why the wavelength of the uncoupled macrodisplacement wave (gray curve in the right panels) appears as larger for more strongly damaged bars, even if it is independent of the damage parameters.

Finally, it is interesting to verify the interference of the micro- and macrodisplacements due to the presence of veering, as already observed in terms of wave components in Fig. 5. Differently from the free wave propagation analysis of Sect. 3, the addition of the boundary conditions allows us to identify the C_1 and C_3 amplitudes which define the relative contribution of the k_1 and k_3 waves on the system response. This implies

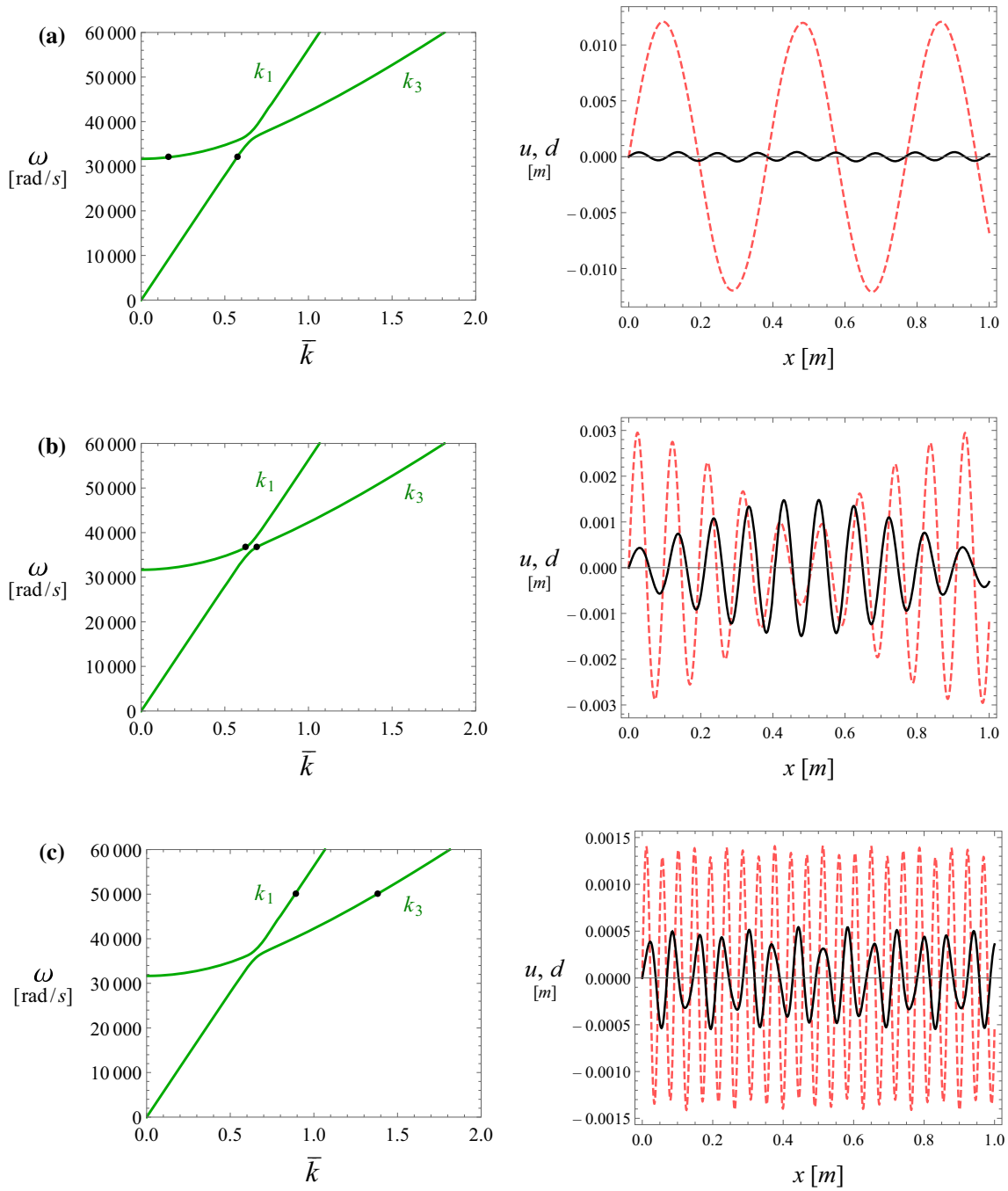

Fig. 14 Frequency spectra and micro- and macrodisplacements for $\Omega = 32000$ rad/s (**a**), $\Omega = \omega(k_{\text{cross}}) = 36677$ rad/s (**b**), $\Omega = 50000$ rad/s (**c**). Black waves: macrodisplacement u; dashed red waves: microdisplacement d. $\delta = 0.05$, $l_c = 0.01$ m, $\rho_m = 100$ m^{-1} (color figure online)

the possibility to reconstruct the actual spatial form of the micro- and macrodisplacements. For the sake of comparison, the parameters are set to the same used to obtain Fig. 5, i.e., $\rho_m = 100$ m^{-1}, $l_c = 0.01$ m and $\delta = 0.05$, while the forcing amplitude is 100 kN. The form of the u and d waves before and after the veering are presented in Fig. 14. Before the veering region, for $\Omega = 32000$ rad/s $\cong \omega_0$ (Fig. 14a), the macro-, u, and micro-, d, waves poorly interfere with each other, despite the presence of coupling, and the u wave is seen to be characterized by a higher wavenumber (i.e., shorter wavelength) with respect to the d wave. It confirms the dominance of the k_3 (k_1) component on the macro- (micro-) displacement before the veering region, as pointed

out also in the previous section. Moreover, the amplitudes of the two waves are evidently different, with the relatively high damage associated with the chosen combination of ρ_m and l_c values entailing a much stronger amplitude of the microwave. For forcing frequency corresponding to the cross-point $\Omega = \omega(k_{\text{cross}}) = 36677$ rad/s (Fig. 14b), wavelengths of u and d waves are almost equal and amplitudes tend to become comparable, highlighting a strong hybridization of the macrodisplacement u which is deeply influenced by the microdisplacement d. For higher forcing frequencies, after the veering occurrence ($\Omega = 50000$ rad/s, Fig. 14c), the microdisplacement d is associated with short wavelength (corresponding to the higher wavenumber branch k_3), while the macrodisplacement is dominated by the k_1 component. However, the distortion of the macrodisplacement waveform due to coupling is still evident. As a minor comment, waves shown in Fig. 14 are studied with respect to a dimensional unitary domain, differently from what done in Fig. 13. This is admissible because the relevant analyses are developed for fixed microcrack density, corresponding to fixed length of the periodic cell, so that the qualitative behavior is not altered by the dimensional representation.

5 Conclusions

The dynamical analysis of a microcracked bar characterized by a uniform distribution of fibers and cracks is performed in order to discuss the effects of damage on the behavior of propagating waves. The considered multifield model is derived from a generalized continuum formulation and accounts for the presence of the microstructure by adding a microdisplacement field, that in a smeared sense represents distribution of microcracks in the bar, to the standard macrodisplacement field. Moreover, a constitutive multiscale description accounts for the material micromodel organization through internal parameters representing cracks density and length.

In terms of wave propagation analysis, the microstructure presence is revealed by the well-known dispersion effects, which are in turn influenced by the features of the microstructure itself. To examine this relation, the dispersion properties of a physically based microcracked bar are extensively investigated, considering varying intensity of coupling between macro- and microdisplacements, as well as different levels of damage.

The outcomes highlight the occurrence of the veering phenomenon associated with the presence of coupling, which entails a strong hybridization of the macrodisplacement, deeply influenced by the microdisplacement. The behavior can be recognized in free wave propagation regime, with the transfer of energy from the harmonic wave contributions of the macrodisplacement to the corresponding ones of the microdisplacement. Moreover, when considering the real sample case of harmonically excited long bar, the evident distortion of the macrodisplacement waveform confirms the role played by the coupling.

The free and forced wave propagation is seen to be strongly influenced also by the micromodel descriptors representing density and length of the microcracks. Besides sensibly reducing the acoustic velocity, the damage parameters prove to meaningfully alter shape, velocity, and actual occurrence of propagating waves. In particular, the influence of damage parameters on the cutoff frequency and on the wavenumbers around the veering region is analytically described and clearly represented by means of several behavior charts. Interestingly, strongly coupled and highly damaged models can undergo a meaningful qualitative change in the dynamical response when the acoustic frequency (or velocity) curve falls to zero, corresponding to the arise of a band gap precluding propagation. From a practical viewpoint, the presented analyses provide an accurate phenomenological description of the model behavior which can furnish useful hints to interpret the response of one-dimensional structures with widespread damage.

Acknowledgements This research was supported by the Italian Ministry of University and Research, P.R.I.N. 2015, Project 2015JW9NJT Advanced mechanical modeling of new materials and structures for the solution of 2020 Horizon challenges, Sapienza Research Unit (Grant B86J16002300001), and by Sapienza University, Grant 2016 (B82F16005920005).

References

1. Rapaport, D.C., Rapaport, D.C.R.: The Art of Molecular Dynamics Simulation. Cambridge University Press, Cambridge (2004)
2. Suzuki, T., Takeuchi, S., Yoshinaga, H.: Dislocation Dynamics and Plasticity. Springer, Berlin (1991)
3. Beran, M.J., McCoy, J.J.: Mean field variations in a statistical sample of heterogeneous elastic solids. Int. J. Solids Struct. **6**(8), 1035–1054 (1970)
4. Sanchez-Palencia, E., Zaoui, A.: Homogenization Techniques for Composite Media. Lecture Notes in Physics. Springer, Berlin (1987)

5. Blanc, C., Le Bris, C., Lions, P.L.: From molecular models to continuum mechanics. Arch. Ration. Mech. Anal. **164**(4), 341–381 (2002)
6. Fago, M., Hayes, R.L., Carter, E.A., Ortiz, M.: Atomistic/continuum coupling in computational materials science. Model. Simul. Mater. Sci. Eng. **11**, R33–R68 (2005)
7. Sadowski, T., Trovalusci, P.: Multiscale Modeling of Complex Materials: Phenomenological, Theoretical and Computational Aspects. CISM Courses and Lectures. Springer, Wien (2014)
8. Capriz, G.: Continua with Microstructure. Springer, Berlin (1989)
9. Eringen, A.C.: Microcontinuum Field Theories. Springer, New York (1999)
10. Gurtin, M.E.: Configurational Forces as Basis Concept of Continuum Physics. Springer, Berlin (2000)
11. Altenbach, J., Altenbach, H., Eremeyev, V.A.: On generalized Cosserat-type theories of plates and shells: a short review and bibliography. Arch. Appl. Mech. **80**, 73–92 (2010)
12. Altenbach, H., Eremeyev, V.A. (eds.): Generalized Continua from the Theory to Engineering Application. CISM Courses and Lectures. Springer, Berlin (2013)
13. Kunin, I.A.: Elastic Media with Microstructure-I. One-Dimensional Models. Springer, Berlin (1982)
14. Trovalusci, P.: Molecular approaches for multifield continua: origins and current developments. In: Multiscale Modeling of Complex Materials, pp. 211–278. Springer (2014)
15. Eringen, A.C.: Nonlocal Continuum Field Theories. Springer, New York (2002)
16. Smyshlyaev, V.P., Cherednichenko, K.D.: On rigorous derivation of strain gradient effects in the overall behaviour of periodic heterogeneous media. J. Mech. Phys. Solids **48**, 1325–1357 (2000)
17. Peerlings, R.H.J., Fleck, N.A.: Computational evaluation of strain gradient elasticity constants. Int. J. Multiscale Comput. Eng. **2**, 599–619 (2004)
18. Bacigalupo, A., Gambarotta, L.: Second-order computational homogenization of heterogeneous materials with periodic microstructure. Zeitschrift für Angewandte Mathematik und Mechanik **90**(10–11), 565–578 (2010)
19. Trovalusci, P., Masiani, R.: Material symmetries of micropolar continua equivalent to lattices. Int. J. Solids Struct. **36**(14), 2091–2108 (1999)
20. Forest, S., Pradel, F., Sab, K.: Asymptotic analysis of heterogeneous cosserat media. Int. J. Solids Struct. **38**, 4585–4608 (2001)
21. Onck, P.R.: Cosserat modeling of cellular solids. Comptes Rendus Mécanique **330**, 717–722 (2002)
22. Trovalusci, P., Masiani, R.: Non-linear micropolar and classical continua for anisotropic discontinuous materials. Int. J. Solids Struct. **40**, 1281–1297 (2003)
23. Forest, S.: Micromorphic approach for gradient elasticity, viscoplasticity, and damage. J. Eng. Mech. **135**(3), 117–131 (2009)
24. Wang, X., Lee, J.D.: Micromorphic theory: a gateway to nano world. Int. J. Smart Nano Mater. **1**(2), 115–135 (2010)
25. Trovalusci, P., Pau, A.: Derivation of microstructured continua from lattice systems via principle of virtual works. The case of masonry-like materials as micropolar, second gradient and classical continua. Acta Mech. **225**(1), 157–177 (2014)
26. Trovalusci, P., Ostoja-Starzewski, M., De Bellis, M.L., Murrali, A.: Scale-dependent homogenization of random composites as micropolar continua. Eur. J. Mech. A Solids **49**, 396–407 (2015)
27. Trovalusci, P., De Bellis, M.L., Masiani, R.: A multiscale description of particle composites: from lattice microstructures to micropolar continua. Compos B Eng. **128**, 164–173 (2017)
28. Trovalusci, P., Augusti, G.: A continuum model with microstructure for materials with flaws and inclusions. Journal de Physique IV **Pr8**, 383–390 (1998)
29. Sansalone, V., Trovalusci, P., Cleri, F.: Multiscale modelling of materials by a multifield approach: microscopic stress and strain distribution in fiber-matrix composites. Acta Materialia **54**(13), 3485–3492 (2006)
30. Sansalone, V., Trovalusci, P.: A numerical investigation of structure-property relations in fibre composite materials. Int. J. Multiscale Comput. Eng. **5**(2), 141–152 (2007)
31. Trovalusci, P., Rega, G.: Elastic waves in heterogeneous materials as in multiscale-multifield continua. Proc. Estonian Acad. Sci. Phys. Math. **56**(2), 100–107 (2007)
32. Trovalusci, P., Varano, V., Rega, G.: A generalized continuum formulation for composite materials and wave propagation in a microcracked bar. J. Appl. Mech. **77**(6), 061002–1/11 (2010)
33. Trovalusci, P., Varano, V.: Multifield continuum simulations for damaged materials: a bar with voids. Int. J. Multiscale Comput. Eng. **9**(5), 599–608 (2011)
34. Berezovski, A., Engelbrecht, J., Salupere, A., Tamm, K., Peets, T., Berezovski, M.: Dispersive waves in microstructured solids. Int. J. Solids Struct. **50**(11–12), 1981–1990 (2013)
35. Berezovski, A., Yildizdag, M.E., Scerrato, D.: On the wave dispersion in microstructured solids. Continuum Mech. Thermodyn. 1–20 (2018)
36. Fish, J., Chen, W., Nagai, G.: Non-local dispersive model for wave propagation in heterogeneous media: one-dimensional case. Int. J. Numer. Methods Eng. **54**, 331–346 (2002)
37. Wang, Z.P., Sun, C.T.: Modelling micro-inertia in heterogeneous materials under dynamic loading. Wave Motion **36**, 473–485 (2002)
38. Sluys, L.J., de Borst, R., Mühlhaus, H.-B.: Wave propagation, localization and dispersion in a gradient-dependent medium. Int. J. Solids Struct. **30**, 1153–1171 (1993)
39. Metrikine, A.V., Askes, H.: One-dimensional dynamically consistent gradient elasticity models derived from a discrete microstructure. Part 1: generic formulation. Eur. J. Mech. A Solids **21**, 555–572 (2002)
40. Metrikine, A.V.: On causality of the gradient elasticity models. J. Sound Vib. **297**, 727–742 (2006)
41. Papargyri-Beskou, S., Polyzos, D., Beskos, D.E.: Wave dispersion in gradient elastic solids and structures: a unified treatment. Int. J. Solids Struct. **46**, 3751–3759 (2009)
42. Erofeyev, V.I.: Wave Processes in Solids with Microstructure. World Scientific, Singapore (2003)
43. Engelbrecht, J., Berezovski, A., Pastrone, F., Braun, M.: Waves in microstructured materials and dispersion. Philos. Mag. **85**(33–35), 4127–4141 (2005)

44. Ván, P., Berezovski, A., Engelbrecht, J.: Internal variables and dynamic degrees of freedom. J. Non-Equilib. Thermodyn. **33**, 235–254 (2008)
45. Berezovski, A., Engelbrecht, J., Maugin, G.A.: Generalized thermomechanics with internal variables. Arch. Appl. Mech. **81**, 229–240 (2011)
46. Bacigalupo, A., Lepidi, M.: Acoustic wave polarization and energy flow in periodic beam lattice materials. Int. J. Solids Struct. **147**, 183–203 (2018)
47. Berezovski, A., Engelbrecht, J., Berezovski, M.: Waves in microstructured solids: a unified viewpoint of modeling. Acta Mech. **220**(1–4), 349–363 (2011)
48. Peets, T., Randrüüt, M., Engelbrecht, J.: On modelling dispersion in microstructured solids. Wave Motion **45**(4), 471–480 (2008)
49. Askes, H., Metrikine, A.V.: One-dimensional dynamically consistent gradient elasticity models derived from a discrete microstructure. Part 2: static and dynamic response. Eur. J. Mech. A Solids **21**, 573–588 (2002)
50. Sansalone, V., Trovalusci, P., Cleri, F.: Multiscale modeling of composite materials by a multifield finite element approach. Int. J. Multiscale Comput. Eng. **3**(4), 463–480 (2005)
51. Mindlin, R.D.: Micro-structure in linear elasticity. Arch. Ration. Mech. Anal. **16**(1), 51–78 (1964)
52. Madeo, A., Neff, P., Ghiba, I.-D., Placidi, L., Rosi, G.: Wave propagation in relaxed micromorphic continua: modeling metamaterials with frequency band-gaps. Continuum Mech. Thermodyn. **27**(4–5), 551–570 (2015)